Vietnam Journal of Science and Technology
DOI: https://doi.org/10.15625/2525-2518/23285

Synthesis of copper benzene 1,3,5-tricarboxylate (CuBTC)/*Macadamia* biochar composite for adsorption of oxytetracycline in water

Thu Phuong Nguyen[1], Thi Hai Do[2], Hong Nam Nguyen[1], Phuong Thu Le[1], Tien Le[1], Quoc Nghi Pham[3], Phu Nhuan Pham[4], Thi Mai Thanh Dinh[1,*]

[1]*University of Science and Technology of Hanoi, Vietnam Academy of Science and Technology, 18 Hoang Quoc Viet, Nghia Do Ward, Ha Noi, Viet Nam*
[2]*Hanoi University of Mining and Geology, 18 Pho Vien Street, Dong Ngac Ward, Ha Noi, Viet Nam*
[3]*Université Paris-Saclay, CNRS, ICMMO, 91405 Orsay, France*
[4]*University of Engineering and Technology, Vietnam National University, 144 Xuan Thuy, Cau Giay Ward, Ha Noi, Viet Nam*

[*]Email: *dinh-thi-mai.thanh@usth.edu.vn*

Received: 12 August 2025; Accepted for publication: 20 November 2025

Abstract. With the increasing number and complexity of emerging pollutants in water, such as antibiotics, the development of new materials with high adsorption capacity has garnered significant research interest. In this study, a CuBTC/biochar composite derived from macadamia was synthesized via the hydrothermal method. The synthesized composite combined biochar microstructure with cubic and rod-like CuBTC nanostructures, enhancing the overall adsorption performance. Energy Dispersive X-ray (EDX) analysis confirmed the presence of Cu, O, and C elements, while Fourier Transform Infrared (FTIR) spectra revealed characteristic peaks corresponding to both CuBTC and biochar. X-ray Diffraction (XRD) patterns identified the 3 Dimensional (3D) crystalline phase of CuBTC, and it was observed that the hydrothermal process reduced the specific surface area of the biochar. Based on the material properties and initial adsorption results, a CuBTC/biochar ratio of 1:1 was selected for further investigation in the treatment of oxytetracycline. The optimal adsorption conditions were determined to be 0.1 g of adsorbent, 1 hour of contact time, and an initial pH of 6. The adsorption process followed the pseudo-first-order and Redlich-Peterson models, with a maximum adsorption capacity of 34 $mg.g^{-1}$ as described by the Langmuir model. The negative values of standard Gibbs free energy change (ΔG) and enthalpy change (ΔH) indicated that the process is spontaneous and exothermic. The adsorption mechanism involves both physical and chemical interactions, including pore filling, electrostatic attraction, π-π interactions, hydrogen bonding, and surface complexation. Remarkably, after one year, despite a 38-fold decrease in the specific surface area of the composite, the material retained nearly 80 % of its adsorption efficiency. These findings highlight the potential of combining macadamia biochar derived from abundant solid waste sources, durable structure and high carbonization efficiency, with metal-organic frameworks such as CuBTC to develop synergistic materials for the removal of emerging pollutants like oxytetracycline antibiotics.

Keywords: CuBTC, biochar, oxytetracycline, adsorption, hydrothermal.

UNCORRECTED PROOF

Classification numbers: 2.9.4, 3.4.2

1. INTRODUCTION

Environmental pollution caused by oxytetracycline (OTC) - a broad-spectrum antibiotic belonging to the tetracycline group - has become a serious concern, particularly in aquatic environments. Widely used in livestock and aquaculture, OTC is poorly degradable and is typically excreted in urine in its uncharged form. This facilitates its entry into natural water bodies such as rivers, lakes, and reservoirs, where it can negatively impact aquatic microorganisms and ecosystems [1]. A study by Kolar *et al.* [1] demonstrated the significant toxicity of OTC to photosynthetic aquatic microorganisms, such as *Pseudokirchneriella subcapitata*, with a 72-hour EC_{50} (half maximal effective concentration) of 1.04 $mg{\cdot}L^{-1}$. Furthermore, OTC was shown to adversely affect activated sludge - an essential component of wastewater treatment systems - with an EC_{50} of 17.9 $mg{\cdot}L^{-1}$. This problem is exacerbated by the fact that current wastewater treatment technologies are often ineffective at completely removing antibiotics like OTC [2]. As a result, residual OTC in aquatic environments can lead to the development of antibiotic-resistant bacteria, alter microbial community structures, and pose significant threats to human health [3].

CuBTC, also known as HKUST-1 (Hong Kong University of Science and Technology -1), is a metal-organic framework (MOF) characterized by a highly porous three-dimensional structure composed of Cu^{2+} ions in paddlewheel coordination linked to BTC (benzene-1,3,5-tricarboxylate) ligands. This architecture provides a large surface area and well-defined pore structure, making CuBTC an effective adsorbent for trace organic pollutants, including antibiotics [4–6]. Notably, Roy *et al.* [4] reported that CuBTC not only adsorbs pharmaceutical pollutants such as OTC from wastewater but can also act as a photocatalyst under visible light, promoting the degradation of antibiotic molecules. The removal mechanism involves both adsorption within the porous framework and photodegradation via reactive radicals (•OH, O_2•-) generated through photoexcitation. Furthermore, CuBTC can undergo post-synthetic modifications, enabling the incorporation of catalytic or optical functionalities, thereby expanding its applications in environmental remediation and gas separation [4]. Given its relatively simple synthesis, the use of environmentally friendly precursors, and multifunctional properties, CuBTC is considered one of the most promising MOFs for the treatment of water pollution caused by pharmaceuticals and antibiotics.

Biochar is a carbon-rich material produced through the pyrolysis of biomass under anaerobic conditions. Among various biomass sources, macadamia shells - an agricultural by-product rich in lignin and carbon - are considered ideal feedstock for biochar production due to their durable structure and high carbonization efficiency [7]. Similar to other types of biochar, macadamia shell-derived biochar possesses a high surface area, porous structure, and cation exchange capacity, making it highly effective for adsorbing organic pollutants such as pesticides, antibiotics, and heavy metals (e.g., Pb, Cd, Zn) in soil and water environments. According to Beesley *et al.* [8], biochar not only reduces the mobility and bioavailability of contaminants but also improves soil structure, enhances water retention, and supports ecosystem restoration in degraded or polluted land areas. Importantly, the adsorption efficiency of biochar is significantly influenced by the type of biomass used and the pyrolysis temperature. Biochars produced at pyrolysis temperatures between 400 - 600 °C generally exhibit good adsorption efficiency due to their high degree of carbonization combined with the presence of amorphous organic matter, which facilitates strong interactions with pollutants.

UNCORRECTED PROOF

CuBTC/biochar composites were first synthesized via the hydrothermal method in 2023 using $Cu(NO_3)_2$ and bamboo-derived biochar, treated at 140 °C for 24 hours, and applied for toluene adsorption. The resulting CuBTC/biochar composite (4:1 ratio) exhibited a high specific surface area of 728.5 $m^2 \cdot g^{-1}$ [9]. Another study synthesized CuBTC-impregnated, boron-doped biochar from orange peels using an impregnation method with $Cu(NO_3)_2$ in a solvent mixture (Dimethylformamide (DMF):H_2O:Ethanol (EtOH) in a 1:1:1 ratio) for ammonia (NH_3) capture, yielding a material with a surface area of 674.31 $m^2 \cdot g^{-1}$ at a CuBTC/biochar ratio of 1:2.5 [10]. However, research on synthesizing CuBTC/biochar composites using the solvothermal method and their application in antibiotic adsorption, particularly OTC, remains limited. In detail, the two above studies did not mention the durability and adsorption capacity of CuBTC/biochar composite after a long time. Therefore, in this study, we synthesized a CuBTC/biochar composite from macadamia nut shells via the solvothermal method and evaluated its effectiveness in adsorbing OTC from aqueous solutions.

2. MATERIALS AND METHODS

2.1. Chemical

Benzene-1,3,5-tricarboxylic acid (H_3BTC, analytical grade) was purchased from Merck. Copper(II) sulfate ($CuSO_4$), dimethylformamide (DMF), and ethanol were all of analytical grade and obtained from China.

2.2. Material

Char production was carried out using an electric muffle furnace (Nabertherm LT 24/12/P300). Around 400 g of macadamia nutshells were placed inside a sealed steel container (10 cm height × 20 cm diameter) under a constant nitrogen flow of 3 $L \cdot min^{-1}$. Pyrolysis was conducted at a heating rate of 10 °C·min^{-1} and held at 600 °C for one hour, yielding a uniform char sample for subsequent use. Char activation was performed in a macro-thermogravimetric reactor located at the University of Science and Technology of Hanoi (USTH), as detailed in previous work [11]. For each activation cycle, the reactor was heated to 900 °C. A 5 g portion of macadamia nutshell char was then introduced into the activation zone and exposed to a gas stream consisting of CO_2 (5 $L \cdot min^{-1}$) and steam (150 $g \cdot h^{-1}$) at a total flow rate of 3 $NL \cdot min^{-1}$. Once approximately 50 % of the carbon content was removed, the gas was switched to pure nitrogen to cool the system and prevent oxidation. The resulting activated chars were collected at ambient temperature.

The CuBTC material was synthesized via a solvothermal method. A solvent mixture was prepared in a 1:1:1 volume ratio comprising 21.25 mL of DMF, 21.25 mL of ethanol, and 21.25 mL of deionized (DI) water. Subsequently, 1.1096 g of $CuSO_4$ and 1.2525 g of H_3BTC were dissolved in the solvent mixture. The resulting solution was then subjected to hydrothermal treatment at 85 °C for 24 hours [12]. After the reaction, the solid product was collected, yielding approximately 1.1 g of CuBTC.

To prepare the CuBTC/biochar composite at a 1:1 weight ratio, 1.1 g of macadamia-derived biochar was added directly to the precursor solution containing $CuSO_4$ and H_3BTC. The mixture was stirred and ultrasonicated for 20 minutes before undergoing the same hydrothermal synthesis conditions. By varying the amount of biochar added, CuBTC/biochar composites with

UNCORRECTED PROOF

different weight ratios (CuBTC:biochar = 1:0.5, 1:1, 1:1.5, and 1:2) were successfully synthesized.

2.3. Characterization methods

2.3.1. Characterization techniques

Fourier-transform infrared (FTIR) spectroscopy was conducted to identify functional groups in the materials using a Nicolet iS10 FTIR spectrometer and a Nicolet iS50 system (Thermo Scientific). The microstructural characteristics of the samples were analyzed using X-ray diffraction (XRD) on a Rigaku Miniflex 600 diffractometer equipped with Cu-Kα radiation. Morphology, elemental composition, and elemental mapping of the samples were examined using a JSM-IT800 scanning electron microscope (JEOL, Japan).

The porous characteristics of the materials produced were examined using nitrogen adsorption-desorption measurements. Prior to analysis, the samples were degassed under vacuum at 150 °C for 3 hours. The measurements were performed at 77 K using an ASAP2060 Micrometrics instrument, with relative pressures ranging from 0 to 0.99 (p/p_0). The specific surface area (SSA) and total pore volume were calculated using the Brunauer-Emmett-Teller (BET) method, while the micropore surface area and volume were determined using the t-plot approach based on the adsorption-desorption isotherms.

The X-ray Photoelectron Spectroscopy (XPS) measurements were performed on a Thermo Fisher Scientific spectrometer equipped with a monochromatic Al Kα radiation source ($h\nu$ = 1486.7 eV) and a hemispherical analyzer operated in constant analyzer energy (CAE) mode. The spectra were processed using the CASA XPS software (Clearwater, FL, USA). Survey scans were acquired with a pass energy of 200 eV and a step size of 1 eV, while high-resolution spectra were recorded with a pass energy of 50 eV and a step size of 0.1 eV. A Shirley background was applied, and the peaks were fitted with a mixed Gaussian-Lorentzian function (70/30). The full width at half maximum (FWHM) was constrained according to recommendations in Ref. [13]. All binding energies were calibrated with respect to the adventitious carbon C 1s peak at 284.8 eV. The uncertainty in binding energy determination is ±0.2 eV.

2.3.2. OTC adsorption capacity

To evaluate the adsorption capacity of the synthesized materials toward OTC, batch adsorption experiments were conducted under various conditions. Adsorbent dosages of 10, 50, 80, 100, 120, and 150 mg were added to 20 mL OTC aqueous solutions with initial concentrations of 10, 20, 50, 100, 150, and 200 ppm. The pH of the solutions was adjusted to values of 2, 4, 6, 8, 10, and 12 using HCl or NaOH prior to the adsorption tests. The mixtures were then agitated at different time intervals (0.5, 1, 2, 3, 4, and 5 hours) and at various temperatures (26 °C, 40 °C, and 55 °C) using a shaking incubator. After the designated contact time, the samples were centrifuged and subsequently filtered to separate the solid and liquid phases.

The residual OTC concentrations in the solution were analyzed using a UV-Vis spectrophotometer (UV-Vis Libra S80, Biochrom, UK) at the characteristic absorption wavelength of OTC, with the calibration curve shown in Figure S1. From these measurements, the adsorption efficiency (%) and the adsorption capacity ($mg.g^{-1}$) of the materials were calculated.

UNCORRECTED PROOF

3. RESULTS AND DISCUSSION

3.1. Morphology and surface chemistry

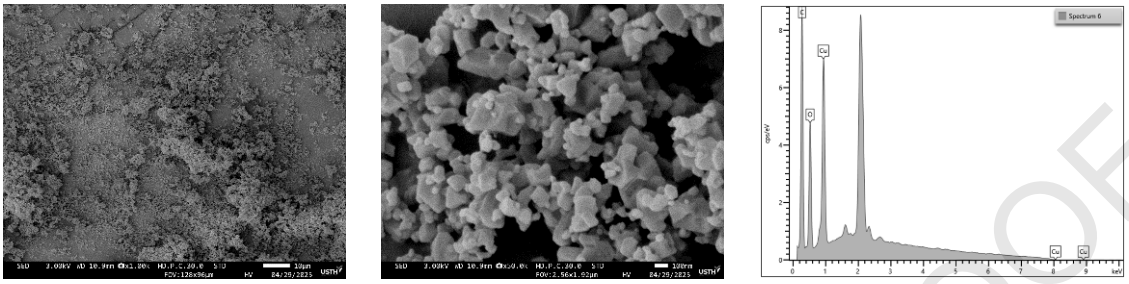

(a) CuBTC

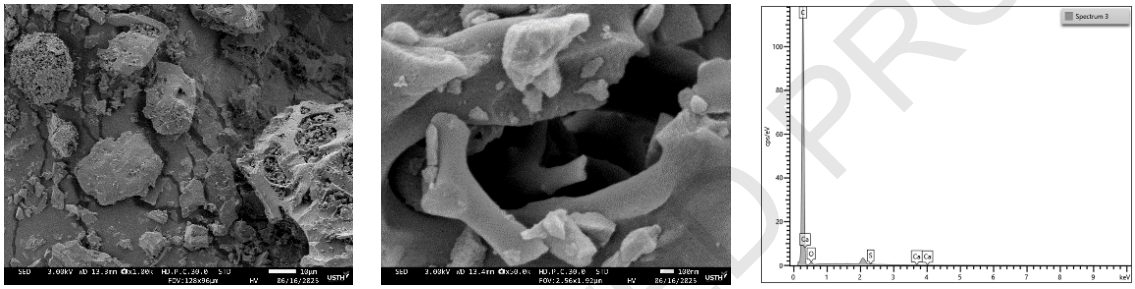

(b) Biochar

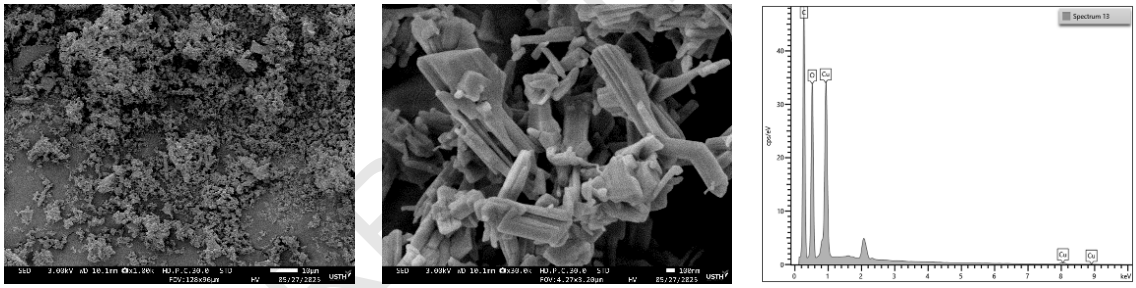

(c) CuBTC/biochar 1:0.5

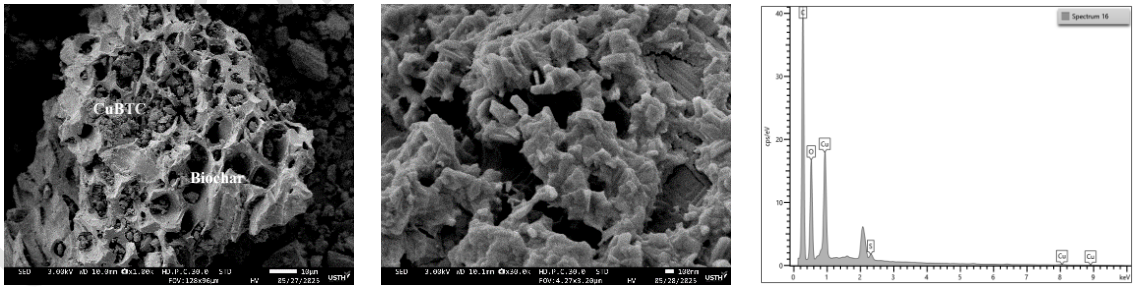

(d) CuBTC/biochar 1:1

UNCORRECTED PROOF

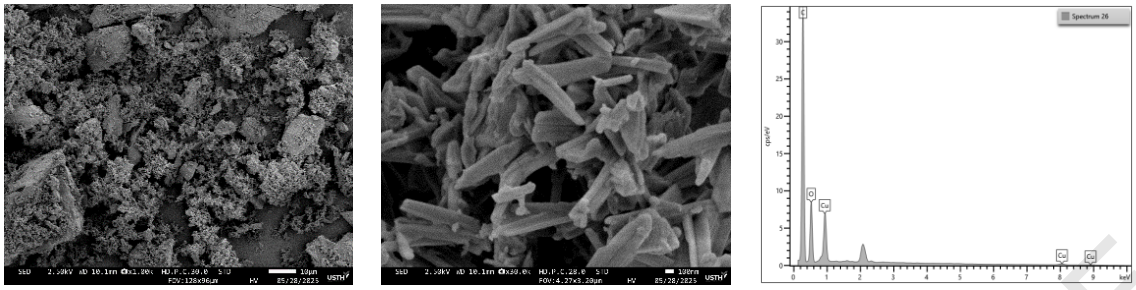

(e) CuBTC/biochar 1:1.5

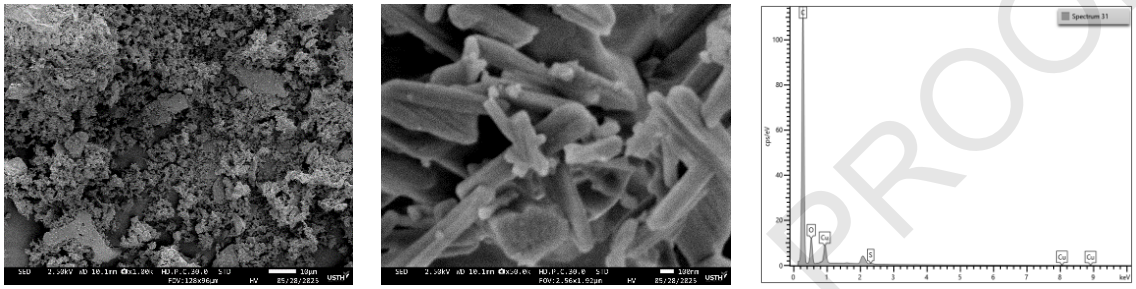

(f) CuBTC/biochar 1:2

Figure 1. FESEM images and EDX spectra of CuBTC, biochar, and CuBTC/biochar composite.

The Field Emission Scanning Electron Microscope (FESEM) images reveal distinct morphological features for each material. The CuBTC sample (Figure 1a) displays well-defined crystalline structures, indicating the formation of a highly ordered MOF. These crystalline particles are visible at both micro and nanoscale levels, demonstrating the uniformity and structural integrity of the CuBTC structure. The inset shows a magnified view, where the individual crystals are clearly observable, further confirming a well-organized network that is characteristic of MOF materials. The particle size is in the 100 nm range, as indicated by the scale bar (nm).

In contrast, the biochar derived from macadamia nut shells (Figure 1b) exhibits a porous and irregular morphology. The surface of the biochar is significantly more heterogeneous, the observed porous structure contributes to a high specific surface area suitable for adsorption. The inset image shows a fragmented and less uniform structure compared to the CuBTC sample, which aligns with the typical morphology of biochar-based adsorbents.

When CuBTC is combined with biochar matrix to form composite materials at various ratios (1:0.5, 1:1, 1:1.5, and 1:2) (Figure 1c-f), significant morphological changes in the CuBTC crystals are observed. Specifically, the originally well-faceted CuBTC crystals become less regular in shape, partially embedded within the porous biochar structure, and in some cases appear smaller or agglomerated. This suggests that the formation of the composite affects the growth and distribution of CuBTC during synthesis or post-synthesis mixing. The surface of the composites becomes rougher and more heterogeneous, indicating a strong physical interaction between CuBTC and biochar. This morphological transformation may increase the number of exposed active sites and enhance mass transfer pathways, both of which are beneficial for adsorption or catalytic applications. The hybrid morphology combines the crystalline structure of CuBTC with the high surface area of biochar, resulting in a synergistic surface architecture.

UNCORRECTED PROOF

This modification not only improves the structural stability of the material but also contributes to its enhanced functional performance in environmental remediation.

The EDX spectra provide further confirmation of the elemental composition of the materials. The CuBTC sample exhibits distinct peaks for carbon (C), oxygen (O), and copper (Cu), which are the key constituents of the CuBTC framework. The macadamia biochar presents strong C and O signals, consistent with its carbon-rich and oxygen-functionalized nature. The presence of oxygen implies the existence of surface functional groups such as -OH, -COOH, or -C=O, commonly found in biochar.

For the CuBTC/biochar composites, the EDX spectra show characteristic peaks of C, O, and Cu, confirming the successful integration of CuBTC into the biochar matrix. Notably, the intensity of Cu peaks increases proportionally with CuBTC amount, reflecting the compositional ratios used. In addition to these major elements, sulfur (S) was detected in all composite samples at a concentration of approximately 0.1 %, with the exception of the CuBTC/biochar 1:1 sample, which exhibited a significantly higher S content of 0.6 % (Table 1). This elevation may be attributed to the optimal interaction interface between CuBTC and biochar at this ratio, leading to enhanced retention of sulfur-containing groups originating from the biochar or residual compounds from pyrolysis. It is also possible that sulfur species were retained due to synthesis-related factors, such as incomplete washing or atmospheric contamination. Although the overall sulfur content remains low, its elevated presence in the 1:1 sample suggests potential contributions to the surface chemistry, possibly enhancing adsorption efficiency through additional hydrogen bonding or dipole-dipole interactions.

Table 1. Element composition and weight percent of materials.

Sample	Cu	C	O	S	Ca
CuBTC	29.5	50.8	19.7	-	-
Biochar	-	97.6	2.2	0.1	0.1
CuBTC/biochar 1:0.5	23.9	50.6	25.4	0.1	-
CuBTC/biochar 1:1	18.8	59.4	21.2	0.6	-
CuBTC/biochar 1:1.5	11.8	68.8	19.3	0.1	-
CuBTC/biochar 1:2	6	81	12.9	0.1	-

The EDX mapping images (Figure 2) confirmed the homogeneous dispersion of key elements such as carbon (C), copper (Cu), oxygen (O), and sulfur (S) throughout the composite matrix. The elemental weight percentages obtained from EDX analysis are summarized in Table 1, where the CuBTC/biochar 1:1 sample exhibited the following elemental distribution: Cu (18.8 %), C (59.4 %), O (21.2 %), and S (0.6 %). These results suggest a successful integration of the MOF structure with biochar, forming a hybrid adsorbent material with well-dispersed active components.

In the FTIR spectra (Figure 3), the CuBTC sample displayed characteristic absorption peaks in the range 1629 cm^{-1} and 1384 cm^{-1}, corresponding to O-C=O functional groups, indicating the presence of these BTC^{3-} groups in the MOF structure. The peak around 574 cm^{-1} corresponds to the Cu-O group in CuBTC, and the peak around 1033 cm^{-1} is related to the C-O group. The macca shell-derived biochar showed a peak around 1635 cm^{-1}, typical of C=C or C=O vibrations, along with another peak at approximately 1396 cm^{-1}, which suggests the presence of C-C groups. Upon combining CuBTC with biochar at different ratios (1:2, 1:1.5, 1:1, and 1:0.5), the spectra revealed significant changes in the intensity and position of these

UNCORRECTED PROOF

peaks, particularly at around 1629 cm^{-1}, 1384 cm^{-1}, and 1033 cm^{-1}. These changes indicate interactions between the CuBTC framework and the functional groups of biochar. The higher biochar content (such as the 1:2 ratio) caused a shift in the C=O absorption (1629 cm^{-1}) to lower wavenumbers, suggesting modifications in the structure of the functional groups. Conversely, the lower biochar content (e.g., 1:0.5 ratio) led to less pronounced shifts but still indicated structural changes, particularly in the MOF network. These findings highlight that the interaction between CuBTC and biochar results in distinct structural modifications.

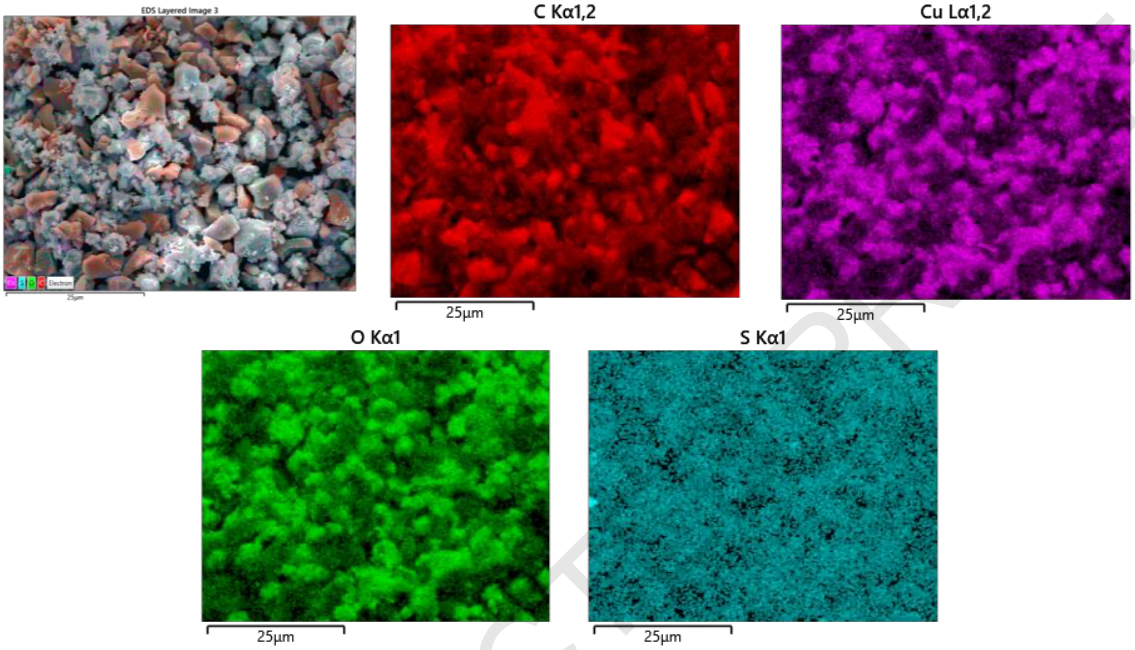

Figure 2. EDX mapping results of CuBTC/biochar 1:1 composite.

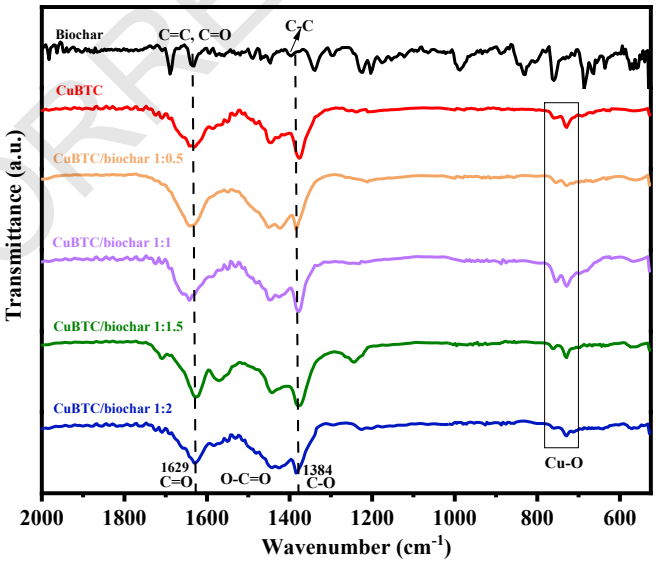

Figure 3. FTIR spectra of the obtained materials.

UNCORRECTED PROOF

3.2. Phase structure

The crystallographic structure and composite formation of CuBTC with macadamia biochar were analyzed using powder XRD (Figure 4). Since the biochar is amorphous, no distinct peaks are observed in its XRD pattern. In contrast, CuBTC exhibits well-defined peaks due to its crystalline cubic structure (space group Fm-3m). The peak positions match those in the reference Crystallography Open Database (COD) entry 96-710-7291. Structurally, each pair of Cu(II) ions is bridged by four carboxylate (μ_2-OCO) groups from separate 1,3,5-benzenetricarboxylate (BTC) ligands, forming square-planar Cu(II) dimers. These dimers further interconnect via the trigonal BTC linkers, resulting in an extended three-dimensional framework. The XRD pattern reveals the presence of prominent peaks corresponding to the (222), (333), (444), (555), (666), (777), and (888) planes, alongside other reflections such as (004), (044), (224), and (135)... The systematic appearance of higher-order reflections (up to (888)) suggests a well-ordered crystalline structure with long-range periodicity. The coexistence of these peaks with lower-index planes may indicate a complex crystallographic orientation. Furthermore, the XRD patterns of all composite materials closely matched that of pure CuBTC, demonstrating that the incorporation of biochar did not adversely affect the crystallization of the MOF. Rietveld refinement using X'Pert HighScore Plus software confirmed the cubic structure in all samples, revealing a composition-dependent lattice response: while CuBTC/biochar at 1:0.5 and 1:1 ratios exhibited slight lattice expansion, CuBTC/biochar at 1:1.5 and 1:2 ratio induced significant lattice contraction. This non-linear variation in unit cell parameters (a, b, c) and volumes (V) (Table 2) demonstrates that biochar incorporation mediates complex structural effects beyond simple pore filling, likely through synergistic mechanisms including lattice strain distortion, modified metal-ligand coordination environments, framework-biochar interfacial interactions, and concentration-dependent stress effects.

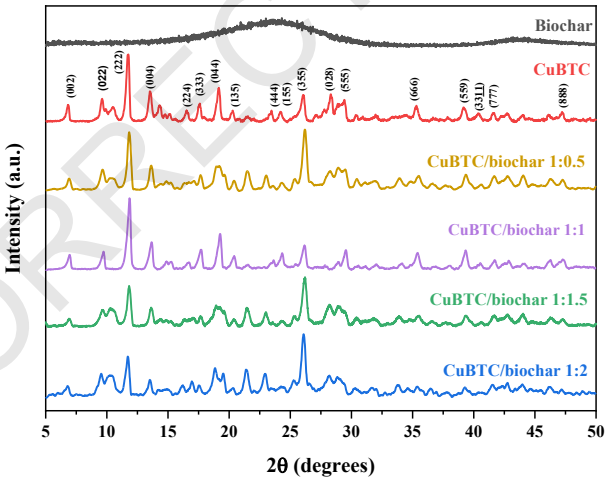

Figure 4. XRD patterns of the obtained materials.

The average crystallite sizes (D_{222}) of the composites were determined using Scherrer's equation $D_{hkl} = \frac{K\lambda}{\beta\, cos(\theta)}$ where K (0.9) is the Scherrer constant (shape factor), λ (0.15418 nm) is the X-ray wavelength of Cu-Kα radiation, β and θ are the full-width half maximum and the Bragg diffraction angle in radians, respectively. The D_{222} crystallite size decreased from 30.38 nm in the pure sample to 23.44 nm in the CuBTC/biochar composite, suggesting that the presence of CuBTC disrupts crystallinity, leading to smaller and less ordered crystallites.

UNCORRECTED PROOF

Notably, the preservation of characteristic CuBTC diffraction patterns confirms that biochar integration maintains MOF crystallinity while compositionally tuning lattice parameters, suggesting an active role of biochar in modulating the framework's structural energetics rather than passive pore occupation.

Table 2. Lattice parameters a,b,c, and crystal volume V of the obtained materials.

Name	A = b = c (Å)	V (Å3)	Crystallite size (nm)
CuBTC	26.41	18420	30.38
CuBTC/biochar 1:0.5	26.46	18525	28.44
CuBTC/biochar 1:1	26.42	18441	24.66
CuBTC/biochar 1:1.5	26.39	18379	24.32
CuBTC/biochar 1:2	26.37	18337	23.44

3.3. Specific surface area and stability

The nitrogen adsorption-desorption isotherms (Figure 5a) and pore size distribution curves (Figure 5b) provide valuable insights into the textural characteristics of CuBTC, macadamia shell-derived biochar, and their composites synthesized at various CuBTC-to-biochar ratios. All samples exhibited type I isotherms, characteristic of predominantly microporous structures. This was further supported by the high specific surface area of micro pore (S_{Micro}) and volume of micro pore (V_{Micro}) values presented in Table 3. Pore size distribution analysis (Figure 5b, Table 3) revealed that all materials had narrow distributions centered around 2-3 nm. The composite materials demonstrated intermediate textural properties relative to the two parent materials. Among the tested samples, pristine biochar exhibited the highest nitrogen adsorption capacity, with a total uptake exceeding 160 $cm^3 \cdot g^{-1}$ STP (Standard Temperature Pressure), corresponding to a specific surface area follows BET (S_{BET}) of 407 $m^2 \cdot g^{-1}$. In contrast, pristine CuBTC showed a lower nitrogen uptake (~110 $cm^3 \cdot g^{-1}$ STP), in agreement with its S_{BET} of 338 $m^2 \cdot g^{-1}$. After hydrothermal treatment, biochar presented a very low nitrogen uptake, about 10 $cm^3 \cdot g^{-1}$ STP, corresponding to a S_{BET} of 28 $m^2 \cdot g^{-1}$. This reduction may be attributed to pore blockage and partial structural collapse of biochar during hydrothermal synthesis. For the composite samples, total nitrogen uptake has values between those of the pure components, and no clear trend was observed with varying CuBTC-to-biochar ratios. This may be due to non-uniform crystal growth and agglomeration at different ratios [14]. Additionally, the low surface area of biochar and potential changes in surface chemistry may have further limited nitrogen accessibility [15]. These combined factors likely contributed to the reduced adsorption capacities and the lack of a proportional relationship with CuBTC content.

The observed reduction in micropore volume in the composites compared to pristine CuBTC can be attributed to the partial pore blockage and the dilution effect of the biochar matrix. Nevertheless, the presence of biochar introduced additional mesoporosity, potentially facilitating the diffusion and adsorption of larger pollutant molecules. Compared to previous studies, pristine CuBTC typically exhibits BET surface areas in the range of 407.28 - 1795.1 $m^2 \cdot g^{-1}$ and CuBTC/biochar synthesized by the hydrothermal method in the range of 674.31 and 728.5 $m^2 \cdot g^{-1}$ [9,10,16], which is significantly higher than the value observed in this work.

The macadamia shell-derived biochar showed surface area and micro-mesoporous characteristics consistent with those of biochars derived from lignocellulosic biomass [17,18]. Similar trends of reduced surface area and increased mesoporosity in MOF-biochar composites

UNCORRECTED PROOF

have been reported in recent studies, emphasizing the synergistic effects that arise from integrating MOFs with carbonaceous supports [11,16].

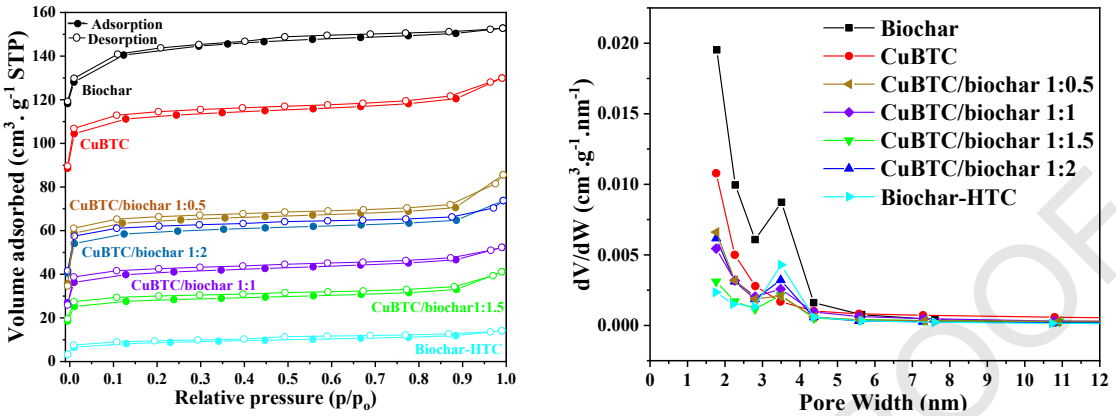

Figure 5. (a) Nitrogen adsorption-desorption isotherms and (b) pore size distribution curves.

Table 3. Specific surface area, pore volume, and pore size of the obtained materials.

	S_{Total} ($m^2 \cdot g^{-1}$)	V_{Total} ($cm^3 \cdot g^{-1}$)	S_{Micro} ($m^2 \cdot g^{-1}$)	V_{Micro} ($cm^3 \cdot g^{-1}$)	S_{Meso} ($m^2 \cdot g^{-1}$)	V_{Meso} ($cm^3 \cdot g^{-1}$)	Poresize (nm)
CuBTC	338	0.19	301.13	0.15	27.31	0.03	2.31
Biochar	407	0.23	351.84	0.19	46.69	0.03	2.30
Biochar HTC	28	0.02	14.25	0.007	10.81	0.01	2.93
CuBTC/biochar 1:0.5	193.4	0.11	167.21	0.08	20.2	0.03	2.54
CuBTC/biochar 1:1	125.1	0.07	98.85	0.05	17.51	0.02	2.49
CuBTC/biochar 1:1.5	86.2	0.05	69.55	0.03	12.2	0.02	2.73
CuBTC/biochar 1:2	179.4	0.1	153.92	0.08	17.72	0.02	2.42

Although the overall porosity of the composite materials decreased compared to the parent materials, the hierarchical porous structure of the CuBTC/biochar composites still offers several advantages. The micropores derived from CuBTC provide a high surface area suitable for the adsorption of small molecules, while the mesopores introduced by biochar enhance mass transport and facilitate the capture of larger organic pollutants. Furthermore, the use of agricultural waste-derived biochar not only reduces production costs but also improves the environmental sustainability of the adsorbent material.

3.4. Impact of aging

To evaluate the long-term stability of the composites, the CuBTC/biochar samples were stored under ambient conditions for one year and re-analyzed. As presented in Table 4 and Figure 6, all aged samples showed a dramatic loss in BET surface area, up to 38-fold compared to the fresh samples.

The specific surface area of CuBTC/biochar 1:1.5 dropped to 4.0 $m^2 \cdot g^{-1}$, and pore volumes decreased to ~0.009 $cm^3 \cdot g^{-1}$. Micropores were nearly eliminated, and only limited mesoporous structures remained (pore sizes ranged from 4.92 to 10.47 nm). This deterioration is likely due to the structural collapse of the MOF framework upon prolonged exposure to atmospheric humidity. CuBTC is known to be moisture-sensitive, and water vapor can hydrolyze the coordination bonds, leading to partial or complete degradation of the porous architecture.

UNCORRECTED PROOF

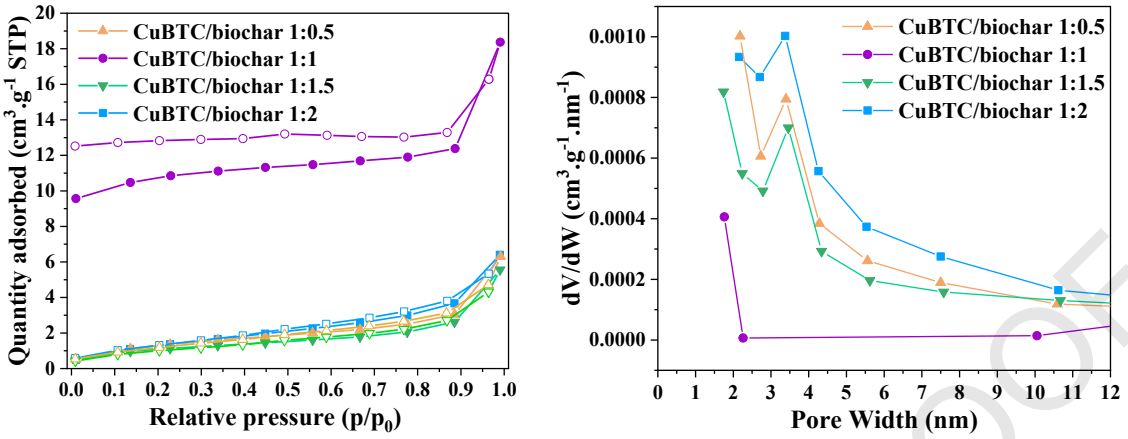

Figure 6. (a) Nitrogen adsorption-desorption isotherms and (b) pore size distribution curves of materials after 1 year.

Table 4. Specific surface area, pore volume, and pore size of the obtained materials after 1 year.

Materials	Specific surface area S_{BET} ($m^2 \cdot g^{-1}$)	Pore volume ($cm^3 \cdot g^{-1}$)	Pore size (nm)
CuBTC/biochar 1:0.5	5.1	0.009	4.92
CuBTC/biochar 1:1	33.5	0.009	5.77
CuBTC/biochar 1:1.5	4.0	0.009	10.47
CuBTC/biochar 1:2	5.3	0.010	5.60

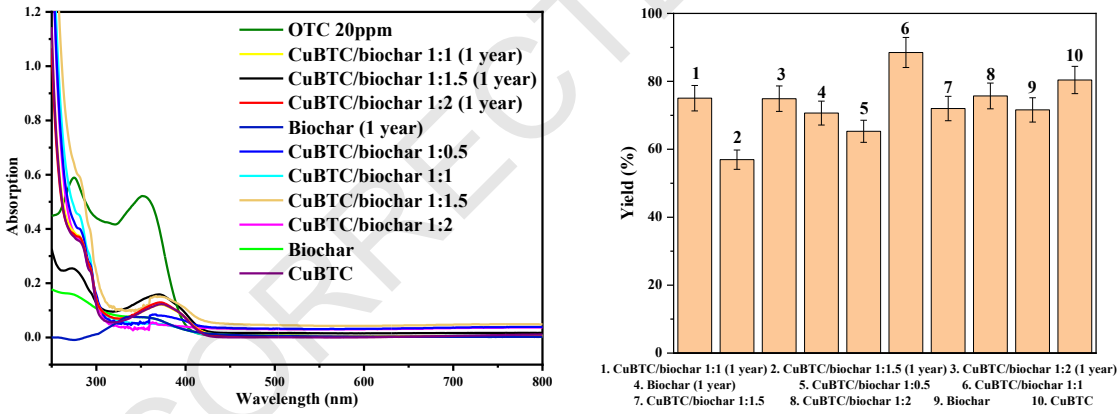

(a) (b)

Figure 7. UV spectra (a) and OTC adsorption efficiency (b) of samples CuBTC/biochar 1:1, CuBTC/biochar 1:1.5; CuBTC/biochar 1:2 after 1 year, and samples CuBTC/biochar 1:0.5; 1:1; 1:1.5; 1:2, biochar, CuBTC at the condition of 0.1 g materials, 20 mL OTC 20 ppm, 1 hour.

Interestingly, despite the pronounced reduction in surface area, the CuBTC/biochar 1:1 composite still retained a high OTC adsorption efficiency of 75 % (Figure 7) under standard conditions (0.1 g adsorbent, 20 mL of 20 ppm OTC, 1 h contact time). This high efficiency indicates that the adsorption mechanism is not solely dependent on surface area or porosity. Other mechanisms, such as surface complexation with copper active sites, π–π stacking interactions, or electrostatic attractions between the antibiotic molecules and functional groups on the carbon matrix, could play significant roles in the retention of performance. These

UNCORRECTED PROOF

findings highlight the composite material's robustness and potential for long-term application in antibiotic removal, even after substantial structural aging. The data suggest that while physical porosity contributes to performance, chemical functionalities and interfacial interactions between CuBTC and biochar are equally critical in maintaining adsorption capabilities over time. From these results, the adsorption is dominated by chemical interactions rather than surface area-controlled physisorption.

The FTIR spectra of samples after 1 year of aging are presented in Figure 8. We can observe that all the samples still have the characteristic peaks, proving the high adsorption ability.

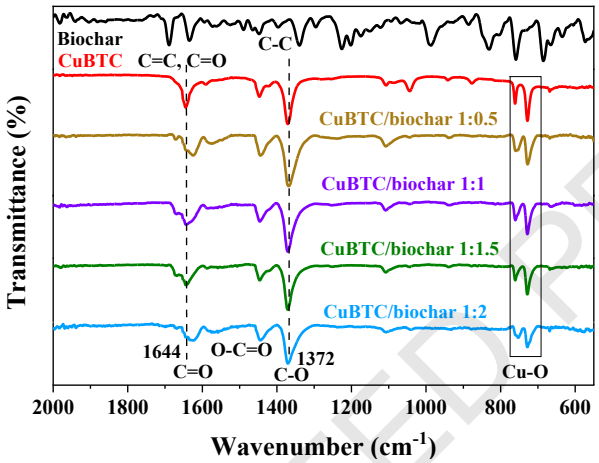

Figure 8. FTIR of samples after 1 year of aging.

3.5. Effect of CuBTC/biochar ratio on OTC adsorption

Table 5. OTC adsorption efficiency of CuBTC/biochar composite with different composition ratios (0.1 g material, 20 mL OTC 20 ppm, 1 hour).

Materials	OTC adsorption efficiency (%)
CuBTC/biochar 1:0.5	65.3
CuBTC/biochar 1:1	88.5
CuBTC/biochar 1:1.5	72.0
CuBTC/biochar 1:2	74.9
Biochar	71.6
CuBTC	80.4

The adsorption efficiency of the synthesized CuBTC/biochar composites with varying weight ratios was investigated under the same conditions: 0.1 g adsorbent, 20 mL of 20 ppm OTC solution, and 1 hour of contact time. As shown in Figure 7 and Table 5, the composite with a CuBTC-to-biochar ratio of 1:1 exhibited the highest removal efficiency, reaching 88.5 %, followed by the 1:2, 1:1.5 and 1:0.5 samples with removal efficiencies of 74.9 %; 72 % and 65.3 %, respectively. The original biochar achieved a removal efficiency of 71.6 %. These results indicate that incorporating an optimal amount of CuBTC into the biochar matrix significantly enhances the OTC adsorption efficiency. The superior efficiency of the 1:1 composite could be attributed to the synergistic effect between the high surface area and porosity of biochar and the active adsorption sites (such as unsaturated Cu^{2+} centers) provided

UNCORRECTED PROOF

by the CuBTC framework. However, excessive biochar content in the 1:2 sample may dilute the CuBTC active sites, while lower biochar content in the 1:0.5 sample may limit surface accessibility and pore diffusion. This phenomenon was observed in the case of CuBTC/biochar used for NH_3 adsorption, where too little CuBTC has insufficient composite enhancement effect, while excessive CuBTC composite may cause blockage of the biochar hole and excessive accumulation [10].

3.6. Effect of adsorbent dosage on OTC removal efficiency

The impact of adsorbent dosage on OTC removal was investigated using the CuBTC/biochar 1:1 composite at dosages ranging from 10 to 150 mg under constant conditions (20 mL of 20 ppm OTC solution, pH_0 = 6, 1-hour contact time). The results are illustrated in Figure 9.

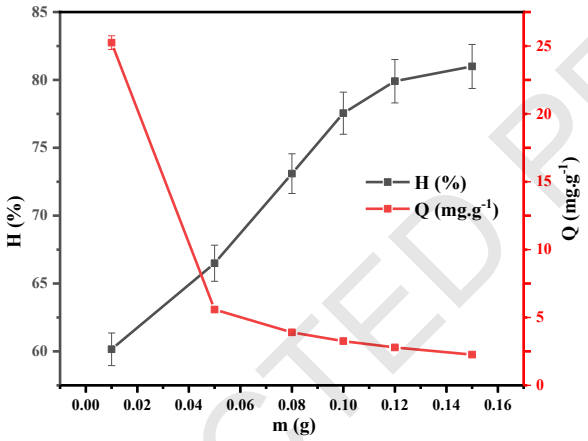

Figure 9. Effect of CuBTC/biochar 1:1 dosage on OTC removal efficiency (*H* %) and adsorption capacity (*Q*) at 20 mL of 20 ppm OTC and 1-hour contact time, pH_0 = 6.

As the adsorbent dosage increased from 10 to 150 mg, the removal efficiency (*H* %) improved significantly, rising from 59.5 % to 83.2 %. This enhancement is attributed to the greater availability of active sites and surface area provided by the increasing amount of adsorbent, which facilitates more extensive interaction with OTC molecules. However, the adsorption capacity (*Q*, $mg \cdot g^{-1}$) showed an inverse trend, decreasing from 25.6 $mg \cdot g^{-1}$ at 10 mg dosage to only 2.2 $mg \cdot g^{-1}$ at 150 mg. This decline is primarily due to the fact that at higher dosages, the number of available adsorption sites surpasses the number of OTC molecules in solution. As a result, the surface of the adsorbent is underutilized, leading to a decrease in *Q* value due to the lower amount of adsorbed OTC per unit mass of adsorbent.

3.7. Effect of contact time and adsorption kinetics

The influence of contact time on OTC adsorption was explored by monitoring the adsorption process over 0.5-5 hours. As depicted in Figure 10a, the adsorption capacity and removal efficiency increased rapidly in the first hour and gradually approached equilibrium thereafter, suggesting a two-stage adsorption mechanism: initial external surface adsorption followed by intraparticle diffusion.

UNCORRECTED PROOF

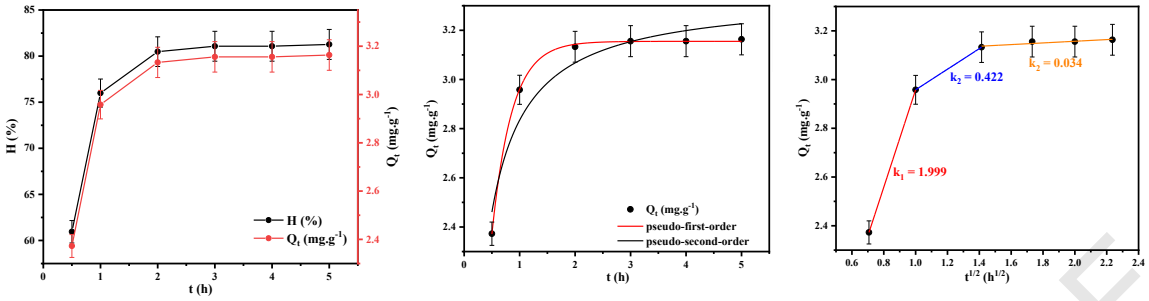

(a) (b) (c)

Figure 10. The variation of efficiency and adsorption capacity follows time (a) Pseudo-first order and pseudo-second order fitting (b), and intra-particle model (c) (0.1 g CuBTC/biochar 1:1; 20 mL OTC 20 ppm, pH_0 = 6).

To further elucidate the kinetics of the adsorption process, the experimental data were fitted using the pseudo-first-order, pseudo-second-order, and intra-particle diffusion models (Figure 10b-c). The kinetic parameters are summarized in Table 6. The pseudo-first-order model provided an excellent fit with a correlation coefficient (R^2 = 0.9996) and a calculated equilibrium adsorption capacity (Q_e,cal = 3.155 mg·g^{-1}) that closely matched the experimental value (Q_e,exp = 3.163 mg·g^{-1}). In contrast, the pseudo-second-order model exhibited a lower correlation (R^2 = 0.9319), and its predicted *Qe,cal* deviated more from the experimental result. The intra-particle diffusion model displayed a linear region but did not pass through the origin, suggesting that while intraparticle diffusion contributes to the rate-limiting step, it is not the sole mechanism controlling adsorption. Instead, the overall process is likely governed by both surface adsorption and pore diffusion.

Table 6. Obtained kinetic parameters from pseudo-first-order (b), pseudo-second-order (b), and Intra-particle models (c).

Parameters	Pseudo-first-order kinetic model	Pseudo-second-order kinetic model	Intra-particle model
$Q_e.exp$ (mg.g^{-1})	3.163	3.163	3.163
$Q_e.cal$ (mg.g^{-1})	3.155	3.342	
K (g.mg^{-1}.min^{-1})	2.784	1.671	k_1 = 1.999 k_2 = 0.422 k_3 = 0.034
R^2	0.99963	0.93194	

3.8. Effect of pH

The point of zero charge (pH_{pzc}) of the CuBTC/biochar 1:1 composite was experimentally determined to be approximately 3.5, as shown in Figure 11. At solution *pH* values below 3.5, the material's surface is positively charged, whereas above 3.5, it becomes negatively charged. The OTC molecule also undergoes speciation with *pH*. At *pH* < 3.5, OTC exists predominantly as a cation [19], leading to electrostatic repulsion with the positively charged adsorbent surface. Consequently, both adsorption capacity (Q) and removal efficiency (H %) at the condition of 0.1 g of materials, contact time of 1 hour, and 20mL of OTC 20ppm are low.

UNCORRECTED PROOF

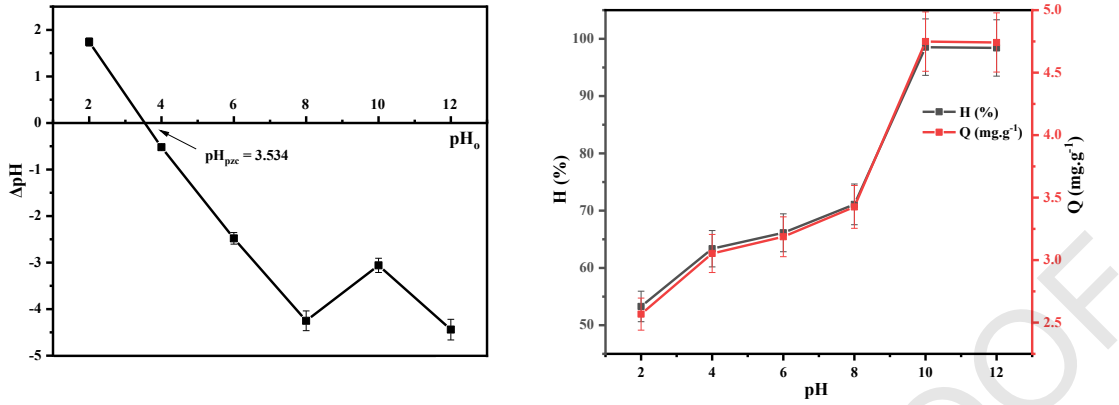

(a) (b)

Figure 11. pH_{pzc} (a) and H and Q changing follow pH (b) (m = 0.1 g; t = 1 hour; 20 mL OTC 20 ppm).

In the *pH* range of 3.5 to 7.49, OTC exists predominantly in its zwitterionic form, carrying both positive and negative charges [19], while the surface of the adsorbent becomes negatively charged. This pH condition promotes moderate electrostatic attraction between OTC and the adsorbent, thereby enhancing adsorption efficiency. At *pH* values above 7.49, OTC transforms to its anionic form [19], while the adsorbent surface remains negatively charged, leading to electrostatic repulsion. Interestingly, both the adsorption capacity (*Q*) and removal efficiency (*H %*) were observed to increase with rising *pH*, reaching their peak at approximately *pH* 10, despite the fact that both OTC and the adsorbent surface carry negative charges at this point.

This result suggests that electrostatic interaction is not the dominant mechanism in this system. Instead, other interactions may play a key role, including: Surface complexation between OTC functional groups (e.g., hydroxyl, carbonyl) and unsaturated Cu^{2+} sites on the CuBTC component. π-π stacking interactions between the aromatic rings of OTC and the graphitic domains in biochar. Hydrogen bonding is facilitated by functional groups on both OTC and the adsorbent surface. A possible role of ligand exchange mechanisms or metal-chelation effects between OTC and Cu sites at higher pH. Moreover, under alkaline conditions, OTC remains in its anionic form, which may enhance its ability to coordinate with Lewis acid sites such as Cu^{2+}. The increase in deprotonation of OTC functional groups at higher pH may also promote stronger bonding to the adsorbent surface. These findings highlight the complexity of the adsorption mechanism and suggest that chemical interactions and specific binding sites are more influential than simple electrostatic attraction in the removal of OTC by the CuBTC/biochar composite.

3.9. Effect of initial concentration, determination of maximum adsorption capacity, and the effect of temperature on OTC adsorption

Figure 12a presents the variation in adsorption capacity and efficiency when the OTC concentration changes. As the OTC concentration increases, the adsorption capacity increases, while the adsorption efficiency decreases.

UNCORRECTED PROOF

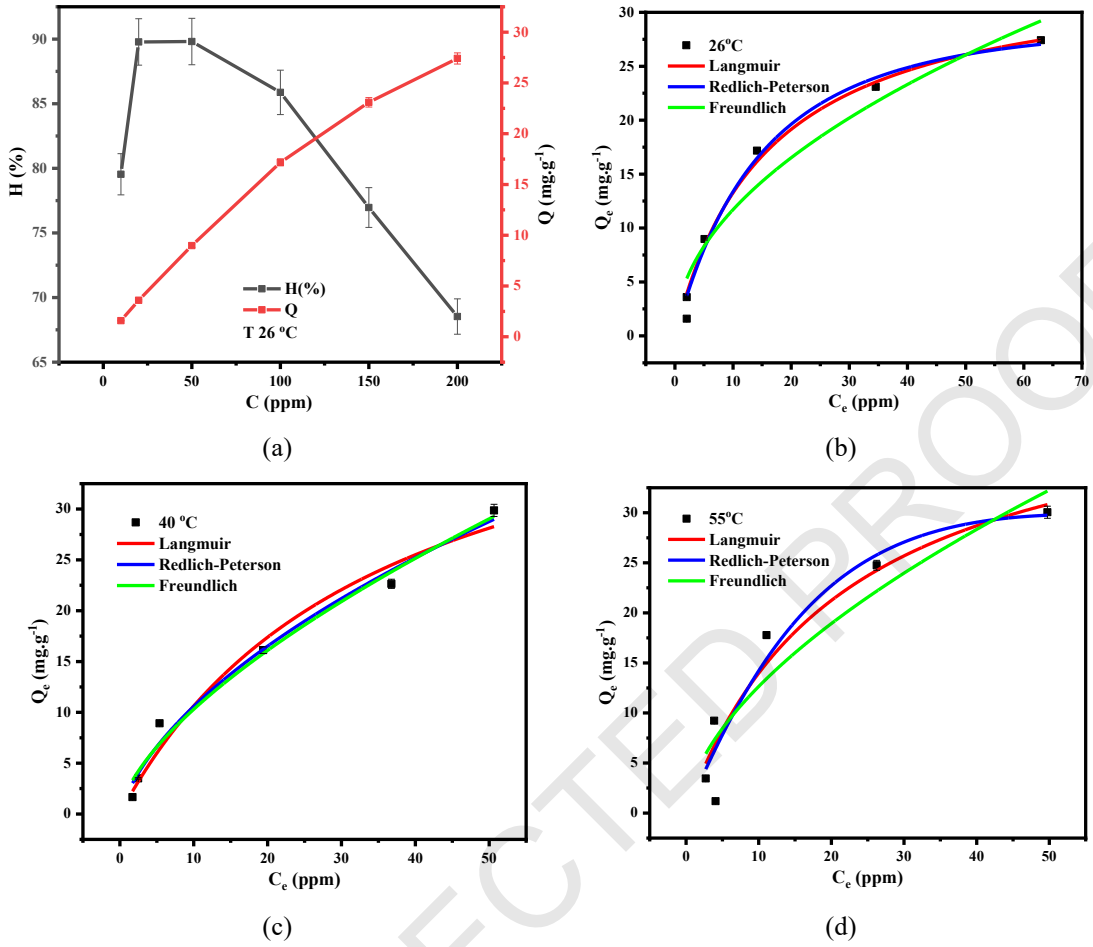

Figure 12. (a) Variation in adsorption capacity and efficiency with changing concentration, fitting experimental data to different models at different temperatures: 26 °C (b), 40 °C (c), and 55 °C (d) (0.1 g, 20 mL OTC, pH_0 = 6, t = 1 hour).

The OTC adsorption isotherms at different temperatures using CuBTC/biochar are illustrated in Figures 12b, c, d. The data are modeled following the Langmuir [20], Freundlich [21], and Redlich-Peterson [22] models, based on the equations:

Langmuir:
$$Q_e = \frac{Q_m K_L Ce}{1 + K_L Ce}$$

Freundlich:
$$Q_e = K_F \, x \, Ce^{1/n}$$

Redlich – Peterson:
$$Q_e = \frac{K_{RP} Ce}{1 + a_{RP} \, x \, Ce^{g}}$$

Table 7 presents the fitted data based on experimental results with changing initial OTC concentrations at different temperatures: 26 °C, 40 °C, and 55 °C. The experimental data follow the Redlich-Peterson model with a higher correlation coefficient (R^2) compared to the Freundlich and Langmuir models. The Redlich-Peterson model is an empirical hybrid of the Freundlich and Langmuir models, often applied to both heterogeneous and homogeneous

UNCORRECTED PROOF

processes. It suggests that the OTC adsorption onto the CuBTC/biochar follows both chemical and physical adsorption mechanisms. The maximum OTC adsorption capacity (Q_{max}) of CuBTC/biochar according to the Langmuir model at 26 ℃ is 34 $mg{\cdot}g^{-1}$. Compared with various materials based on biochar and CuBTC, the Q_{max} of CuBTC/biochar is in the value range of other materials (Table 8).

Table 7. Parameters of the models used to fit the data at different temperatures.

Model	Parameters	299 K	313 K	328 K
Langmuir	QL (mg. g-1)	34.3714	47.79652	44.23175
	KL (L.mg-1)	0.06288	0.02859	0.04619
	R2	0.98723	0.97769	0.92549
Freundlich	KF (L.mg-1)	3.72551	2.33855	3.31089
	nF	2.01158	1.55294	1.71817
	R2	0.94062	0.98525	0.88344
Redlich-Peterson	KRP (L.mg-1)	1.93776	3.40414	1.65284
	aRP (L.mg-1)g	0.03429	0.70986	0.00532
	gRP	1.11745	0.49464	1.48527
	R2	0.9885	0.98623	0.93451

Table 8. Maximum OTC adsorption capacity of other materials.

Materials	S_{BET} ($m^2{\cdot}g^{-1}$)	Q_{max} ($mg{\cdot}g^{-1}$)	Refs.
KOH-modified biochar		10	[23]
Biochar-supported zero-valent iron nanocomposites (biochar from chestnut) $BCFe_{1.5}$	865.86	115.23	[24]
Biochar from maize straw, 600 ℃	3.152	12.02	[25]
Biochar from ginger straw, 600 ℃	16.12	21.25	[26]
Sycamore flock based biochar $SFB_{2\text{-}900}$ (activated agent K_2CO_3, 900 ℃)	1651.27	755.42	[27]
CuBTC/AG (aerogel)	81	316	[28]
CuBTC/biochar	125.1	34	This study

Temperature significantly affects the adsorption process due to it increases the movement of ions in the solution. Therefore, the impact of temperature on OTC adsorption has been investigated. Following kinetics, raising the temperature will increase the diffusion rate of OTC to the surface of CuBTC/biochar, thereby enhancing the adsorption rate. Furthermore, as adsorption and solubility are inversely related, raising the temperature normally raises solubility, which in turn impacts the adsorption capacity. The thermodynamic parameters, including the enthalpy change (ΔH°), entropy change (ΔS°), and standard Gibbs free energy change (ΔG°) of the adsorption process of OTC, are calculated using the van't Hoff equations [23]:

$$\Delta G^o = -RT\ln K^o_{eq} = \Delta H^o - T\Delta S^o$$

$$\ln K^o_{eq} = -\frac{H^0}{R}\ x\frac{1}{T} + \frac{S^0}{R}$$

$$K^{\circ}eq\ [Langmuir] = \frac{K_L\ x\ 1000\ x\ M_{adsorbate}\ x\ [Adsorbate]^o}{\gamma CFX}$$

UNCORRECTED PROOF

$$K^{\circ}eq\ [Freundlich] = \frac{K_F\ x\ 1000\ x\ M_{adsorbate}\ x\ [Adsorbate]^o}{\gamma CFX}$$

$$K^{\circ}eq\ [Redlich - Peterson] = \frac{\sqrt[n_{RP}]{a_{RP}}\ x\ 1000\ x\ M_{adsorbate}\ x\ [Adsorbate]^o}{\gamma CFX}$$

$$[q_e\ (mg{\cdot}g^{-1}),\ C_e\ (mg{\cdot}L^{-1})]$$

where R is the ideal gas constant (8.314 $J{\cdot}mol^{-1}\ K^{-1}$), T is the temperature in Kelvin (K), K^{o}_{eq} is the equilibrium constant. $M_{adsorbate}$ (460.434 $g{\cdot}mol^{-1}$) is the OTC molecular weight, γOTC is the OTC activity coefficient in solution (under dilute conditions, γOTC is considered to be 1), and [Adsorbate] is the standard unit concentration of the adsorbate (~ 1 $mol{\cdot}L^{-1}$). The values of ΔH°, ΔS°, and ΔG° presented in Table 9 are calculated from the slope and the x-intercept of the fit line between LnK^{o}_{eq} and 1/T from Table 9. Negative values of ΔG° and ΔH° indicate that this is an exothermic and spontaneous process.

Table 9. Experimental values of ΔH°, ΔS°, and ΔG°.

T (K)	K°_{eq}	van't Hoff equation	Thermodynamic parameters		
			ΔG ($kJ{\cdot}mol^{-1}$)	ΔH° ($kJ{\cdot}mol^{-1}$)	ΔS° ($J{\cdot}mol^{-1}\ K^{-1}$)
Langmuir Model					
299	28952.09	y = 1059.6x + 6.5212 R^2 = 0.1556	-25.020	-8.810	54.103
313	13163.81		-25.780		
328	21267.45		-26.593		
Freundlich Model					
299	1715351.47	y = 409.8x + 12.851 R^2 = 0.0626	-35.353	-3.407	106.843
313	1076747.931		-36.849		
328	1524446.326		-38.452		
Redlich-Peterson Model					
299	22505.91323	y = 1646.2x + 5.3663 R^2 = 0.026	-27.027	-13.687	44.615
313	230296.5213		-27.651		
328	13554.176		-28.320		

3.10. Change in functional groups of CuBTC/biochar before and after OTC adsorption

Figure 13 shows the FTIR spectra of OTC and sample CuBTC/biochar before and after OTC adsorption at condition: 0.1g materials, 20 mL OTC 20ppm, 1 hours, pHo. CuBTC/biochar after OTC adsorption still has characteristic peaks of CuBTC such as -O-C=O and -Cu-O groups. We can observe that after OTC adsorption, on the spectrum of CuBTC/biochar, some peaks of OTC appear at about 1175 cm^{-1} and 588 cm^{-1}. This proves that OTC was adsorbed on the surface of the CuBTC/biochar materials and clarifies the adsorption mechanism.

INCORRECTED PROOF

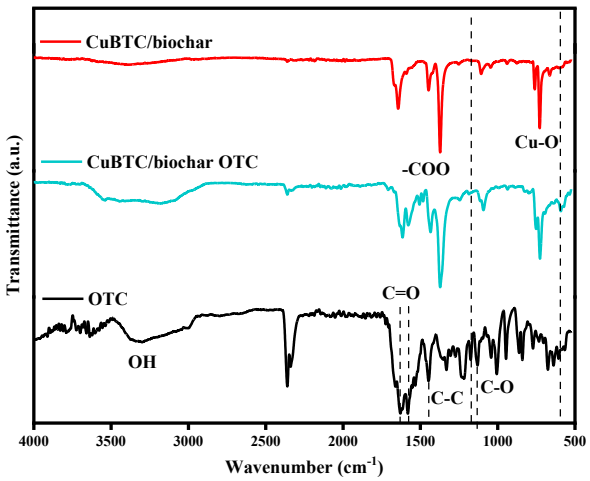

Figure 13. FTIR spectra of OTC and CuBTC/biochar 1:1 before and after OTC adsorption.

3.11. Change in bonds of CuBTC/biochar before and after OTC adsorption

The XPS survey spectra of OTC, CuBTC/biochar 1:1, and CuBTC/biochar 1:1 after OTC adsorption are shown in Figure 14. The main photoelectron lines correspond to C 1s (~284.8 eV) and O 1s (~531-533 eV), which dominate in all samples. In the composite, the presence of copper is confirmed by the Cu 2p region (933-950 eV) and the Cu LMM Auger transition (~568-572 eV). The survey also shows the O KLL Auger feature (975-1000 eV) and the C KLL Auger feature (1190-1220 eV), consistent with the carbonaceous and oxygenated nature of the composite. Before exposure to oxytetracycline, a N 1s signal at ~399-401 eV is already present in the CuBTC/biochar composite, most likely due to residual DMF from the synthesis process, since the synthesis temperature was 85 °C. For this reason, the detailed analysis was focused on the high-resolution C 1s, O 1s, and Cu 2p spectra.

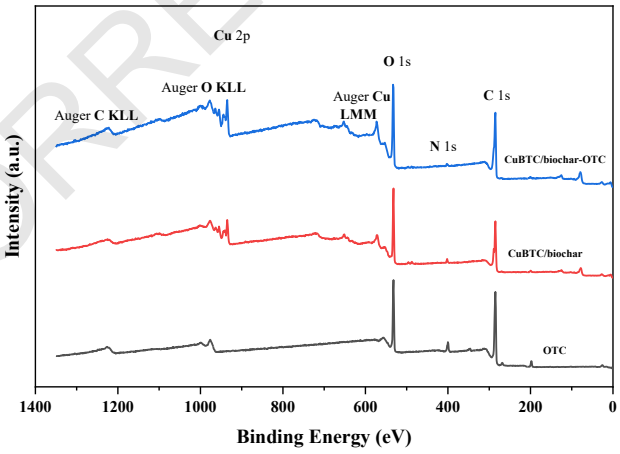

Figure 14. XPS survey scan of (a) OTC and CuBTC/biochar 1:1 before (b) and after (c) adsorption of OTC.

Narrow scans were acquired to probe the carbon environments in OTC, the CuBTC/biochar composite, and the composite after OTC adsorption. For OTC (Figure 15), the C 1s spectrum shows a dominant C–C/C=C contribution at 284.8 eV, together with C–N/C–O at 286.3 eV and two carbonyl signals at 287.2 eV (ketone) and 287.9 eV (amide). A weak π–π*

UNCORRECTED PROOF

satellite is also observed at 290.9 eV. No O–C=O signal is detected, consistent with the absence of carboxylate groups in the OTC molecule [24,29].

In the CuBTC/biochar composite (Figure 15b), C–C/C=C and a shoulder at lower binding energy dominate the spectrum, reflecting the combined contributions of the BTC linker and the graphitic biochar. Oxygenated species are present as C–O/C–N and C=O functionalities, while the O–C=O signal at 288.8 eV is characteristic of the CuBTC carboxylate groups [11]. A weak π–π* shake-up is also present. These features confirm the coexistence of biochar and CuBTC signatures at the surface. Surprisingly, a component at 283.6 eV (18 %) is assigned to reduced sp^2 carbon or possible C-Cu bonding, which is characteristic of the biochar contribution.

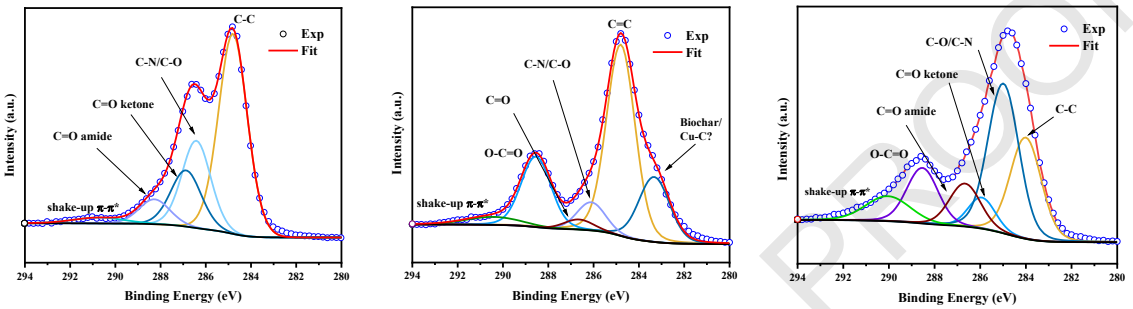

Figure 15. Deconvolution of C 1s core electron spectra (a) OTC and composite CuBTC/biochar 1:1 before (b) and after (c) OTC adsorption.

After OTC adsorption (Figure 15c), the spectrum changes significantly. The C–C/C=C signal decreases, while the C–N/C–O contribution becomes the main feature, indicating the presence of OTC functional groups at the surface. In addition, a clear amide C=O component emerges around 287.9 eV, which serves as a diagnostic fingerprint of OTC. The O–C=O peak of CuBTC remains visible, confirming that the MOF structure is preserved. Together, these changes demonstrate successful OTC adsorption and a surface enrichment in nitrogen- and oxygen-containing groups.

Narrow scans of the O 1s region were collected for OTC, the CuBTC/biochar composite, and the composite after OTC adsorption. For OTC (Figure 16a), the spectrum is described by two main components: carbonyl oxygen at ~531.5 eV (C=O) and oxygen in C–O/OH groups at ~532.7 eV. A small high-binding-energy tail near 533.5 eV is attributed to adsorbed water or surface hydroxyls, in line with earlier XPS analyses of OTC [30]. No signal related to metal–oxygen species is observed, as expected for OTC.

For CuBTC/biochar, the O 1s envelope of the composite (Figure 16b) is deconvoluted into three components at 531.3 eV (47.8 %), 532.0 eV (36.6 %), and 533.2 eV (15.6 %). The lowest-BE (binding energy) component is assigned to carboxylate oxygen coordinated to Cu(II) in the paddle-wheel nodes of CuBTC, consistent with previous reports on HKUST-1 [31]. The feature at ~532.0 eV corresponds to non-coordinated carboxylate oxygen of the BTC linker (O=C–O–) and may also include contributions from C–O/OH groups of the biochar surface. The weak high-BE signal at ~533.2 eV is attributed to adsorbed H_2O or surface hydroxyls. This separation confirms intact Cu–carboxylate coordination together with oxygenated functionalities from the organic linker and the biochar, providing the reference for analyzing OTC adsorption.

After OTC adsorption (Figure 16c), the O 1s spectrum shows clear modifications. The signal at ~532.3 eV also becomes more pronounced, consistent with enrichment in C–O and hydroxyl functionalities from OTC. Meanwhile, the contribution at ~533.3 eV is slightly

UNCORRECTED PROOF

enhanced, indicating additional adsorbed water molecules or hydrogen-bonded OTC species. These changes confirm the presence of OTC at the surface and the development of new interactions between the antibiotic and the oxygenated sites of the composite.

The high-resolution Cu 2p spectra of the CuBTC/biochar composite before and after OTC adsorption are shown in Figure 17. The Cu $2p_{3/2}$ region displays a main peak at ~933.6 eV accompanied by intense satellite features in the 940-945 eV range, which are characteristic of Cu(II) species in paddle-wheel nodes of HKUST-1 [11]. In addition, the presence of a shoulder at slightly lower binding energy (~932.3 eV) suggests a contribution from Cu(I) or metallic Cu(0), consistent with partial reduction of copper during the synthesis or interaction with the biochar support. The Cu $2p_{1/2}$ component is observed at ~953.5 eV, with a similar satellite pattern. The coexistence of Cu(II) with minor Cu(I)/Cu(0) species is fully consistent with previous reports on CuBTC-based composites [31]. After OTC adsorption, the Cu(II) satellites remain clearly visible, confirming the persistence of the MOF structure and the role of Cu(II) sites as the main coordination centers for OTC.

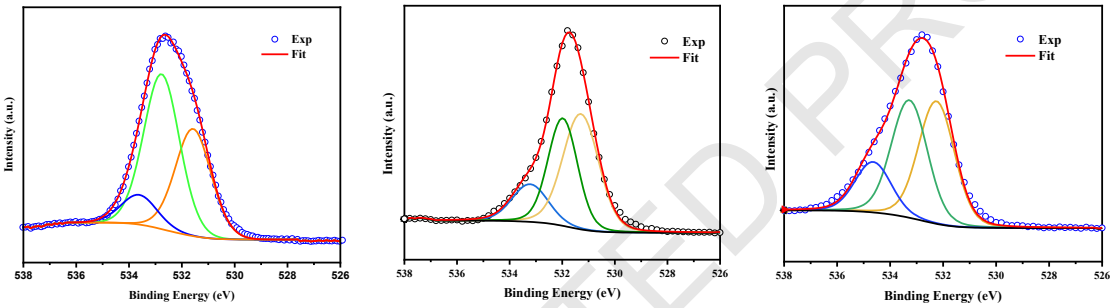

Figure 16. Deconvolution of O 1s core electron spectra (a) OTC and composite CuBTC/biochar 1:1 before (b) and after (c) OTC adsorption.

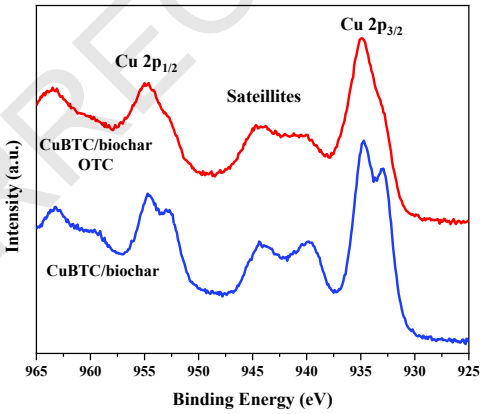

Figure 17. Comparison of Cu 2p core electron spectra of composite CuBTC/biochar 1:1 before (a) and after (b) OTC adsorption.

The XPS results, together with the functional groups present in oxytetracycline, suggest that adsorption occurs mainly through hydrogen bonding between OTC hydroxyl/amide groups and oxygenated sites of biochar, as well as interactions between OTC carbonyl or amine groups and the Cu^{2+} centers of CuBTC. In addition, π–π stacking between the aromatic rings of OTC and those of the BTC linker or graphitic biochar domains likely contributes to stabilization of the adsorbed molecules.

UNCORRECTED PROOF

After OTC adsorption, the Cu 2p peak exhibited a slight positive shift, indicating coordination interactions between Cu centers and oxygen-containing groups of OTC. Meanwhile, the O 1s region showed enhanced signals attributable to –OH and C=O groups, and the C 1s region revealed increased π–π conjugation. These observations confirm that the adsorption process involves not only physical pore filling but also chemical interactions including coordination bonding, hydrogen bonding, and π–π electron interactions.

4. CONCLUSIONS

In this study, a composite material consisting of CuBTC and biochar derived from macadamia nut shells, a sustainable waste source, was successfully synthesized using the hydrothermal method. Although the hydrothermal process led to a reduction in the specific surface area, the incorporation of biochar into the composite structure enhanced the stability of CuBTC in humid atmospheric conditions. Characterization results from FTIR, SEM-EDX, XRD, and BET analyses confirmed the presence of functional groups characteristic of both CuBTC and biochar, the 3D crystalline phase of CuBTC, and the elemental composition of Cu, O, and C. Morphologically, CuBTC appeared as rod- or cube-shaped structures distributed on the surface and within the pores of the biochar matrix. The composite exhibited stable adsorption performance toward OTC, achieving a maximum adsorption capacity of 34 $mg.g^{-1}$. The adsorption behavior followed the pseudo-first-order and Redlich-Peterson kinetic models, and thermodynamic analysis indicated that the process was spontaneous and exothermic. After aging of 1 year, the materials still have a good OTC adsorption efficiency about 75 % showing the long-term stability of composites.

Acknowledgements. This work was supported by the University of Science and Technology of Hanoi (USTH), Vietnam Academy of Science and Technology (VAST) under the NCVCC43.01/25-25 project. The authors would like to thank the Research Group "Sustainable Energy and Environmental Development" (SEED) for their support. The authors are grateful to Dr. Diana Dragoe for conducting the XPS measurements and for her insightful discussions on the precautions necessary for reliable XPS data fitting.

CRediT authorship contribution statement. Thu Phuong Nguyen: Conceptualization, Methodology, Investigation, Formal analysis, Writing – original draft, Writing – review & editing. Thi Hai Do: Methodology, Investigation, Formal analysis. Hong Nam Nguyen: Conceptualization, Formal analysis, Writing – original draft. Phuong Thu Le: Formal analysis, Writing – original draft. Tien Le: Methodology, Formal analysis, Writing – original draft. Quoc Nghi Pham: Formal analysis, Writing – review & editing. Phu Nhuan Pham: Formal analysis. Thi Mai Thanh Dinh: Conceptualization, Funding acquisition, Writing – original draft, Writing – review & editing, Supervision, Project administration.

Declaration of competing interest. The authors declare that they have no known competing financial interests or personal relationships that could have appeared to influence the work reported in this paper.

Data Availability Statement. Data are available upon reasonable request from the corresponding author.

REFERENCES

1. Kolar B., Arnuš L., Jeretin B., Gutmaher A., Drobne D., Durjava M. K. – The toxic effect of oxytetracycline and trimethoprim in the aquatic environment. Chemosphere, **115** (2014) 75–80. https://doi.org/10.1016/j.chemosphere.2014.02.049.

UNCORRECTED PROOF

2. Haque M. A., Rogerson L., Deb Nath N., Haruna S., Ahn J., Johnston T. V., Lin C. S. K., Chong L., Na L., Jang M. J., et al. – Sustainable management and valorization of antibiotic waste. Chem. Eng. J., **498** (2024) 155372. https://doi.org/10.1016/j.cej.2024.155372.
3. Hu Y., Gai N., Yuan Z., Zhou B., Hou R., Yuan R., Chen H. – Ecological effects of antibiotics on aquatic microbial communities: Structure-function response dynamics and multifactorial drivers. Chem. Eng. J., **525** (2025) 169822. https://doi.org/10.1016/j.cej.2025.169822.
4. Roy S., Darabdhara J., Ahmaruzzaman M. – Recent advances in Cu-BTC MOF-based engineered materials for the photocatalytic treatment of pharmaceutical wastewater towards environmental remediation. RSC Sustain., **1** (2023) 1952–1961. https://doi.org/10.1039/D3SU00276D.
5. Yue J., Zheng Q., Ding S., Yin Y., Zhang X., Wang L., Gu Y., Li J., Zhang Y., Shi Y., et al. – Cu–Co bimetallic organic framework as effective adsorbents for enhanced adsorptive removal of tetracycline antibiotics. Sci. Rep., **14** (2024) 17607. https://doi.org/10.1038/s41598-024-67986-8.
6. Sethi P., Barman S., Basu S. – CuBTC–clay composites with tunable ratios for antibiotic removal: Unraveling isotherm, kinetic, and thermodynamic study. Mater. Adv., **6** (2025) 6370–6385. https://doi.org/10.1039/d5ma00639b.
7. Vu L. N., Nguyen T. P., Le P. T., Dinh T. M. T., Nguyen H. N. – Physico-chemical properties of macadamia nut shell post-gasification residues and potential agricultural application. Vietnam J. Sci. Technol., **62** (2024) 58–67. https://doi.org/10.15625/2525-2518/18001.
8. Beesley L., Moreno-Jiménez E., Gomez-Eyles J. L., Harris E., Robinson B., Sizmur T. – A review of biochars' potential role in the remediation, revegetation and restoration of contaminated soils. Environ. Pollut., **159** (2011) 3269–3282. https://doi.org/10.1016/j.envpol.2011.07.023.
9. Zhang J., Shao J., Zhang X., Rao G., Li G., Yang H., Zhang S., Chen H. – Facile synthesis of Cu-BTC@biochar with controlled morphology for effective toluene adsorption at medium–high temperature. Chem. Eng. J., **452** (2023) 139003. https://doi.org/10.1016/j.cej.2022.139003.
10. Xiao J., Zhang Y., Zhang T. C., Wang Y., Yuan S. – Cu_3BTC_2 MOF-impregnated boron-doped biochar derived from orange peels for enhanced NH_3 capture. Appl. Surf. Sci., **635** (2023) 157735. https://doi.org/10.1016/j.apsusc.2023.157735.
11. Nguyen H. N., Nguyen T. P., Le P. T., Tran Q. M., Do T. H., Nguyen T. D., Tran-Nguyen P. L., Tsubota T., Dinh T. M. T. – Investigation on cost-effective composites for CO_2 adsorption from post-gasification residue and metal organic framework. J. Environ. Sci, **148** (2025) 174–187. https://doi.org/10.1016/j.jes.2023.10.022.
12. Su Z., Duan M., Wang Y., Fan H., Tian Z., Chen Z., Yang C., Shangguan J. – In-situ preparation of Cu-BTC modified with organic amines for H_2S removal under ambient conditions. Resour. Chem. Mater., **2** (2023) 143–150. https://doi.org/10.1016/j.recm.2023.03.001.
13. Major G. H., Fairley N., Sherwood P. M. A., Linford M. R., Terry J., Fernandez V., Artyushkova K. – Practical guide for curve fitting in X-ray photoelectron spectroscopy. J. Vac. Sci. Tech. A, **38** (2020) 061203. https://doi.org/10.1116/6.0000377.
14. Singh N., Dalakoti S., Wamba H. N., Chauhan R., Divekar S., Dasgupta S., Aarti – Preparation of Cu-BTC MOF extrudates for CH_4 separation from CH_4/N_2 gas mixture. Microporous Mesoporous Mater., **360** (2023) 112723. https://doi.org/10.1016/j.micromeso.2023.112723.
15. Skic K., Adamczuk A., Gryta A., Boguta P., Toth T., Jozefaciuk G. – Surface areas and adsorption energies of biochars estimated from nitrogen and water vapour adsorption isotherms. Sci. Rep., **14** (2024) 30362. https://doi.org/10.1038/s41598-024-81030-9.
16. Mai N. T., Mai P. T., Dinh T. T. M., Nguyen D. V., Nguyen P. T., Nguyen N. H. – Towards cost-effective CO_2 adsorption materials: Case of CuBTC - Hydrochar composite. Mater. Today Commun., **38** (2024) 107619. https://doi.org/10.1016/j.mtcomm.2023.107619.
17. Nguyen H. N., Bui T. P., Tran T. T. H., Nguyen T. H. H., Le P. T. – Bamboo-derived biochar as an efficient adsorbent for oxytetracycline removal from water. Adv. Bamboo Sci., **11** (2025) 100144. https://doi.org/10.1016/j.bamboo.2025.100144.
18. Hong Nam N., Phuong Thu L., Thu Phuong N., Thi Hai D., Trung Dung N., Thi Mai Thanh D., Quang Minh T. – Removing emerging organic pollutants (oxytetracycline) by engineered biochars originated from agricultural wastes. Environ. Prog. Sustainable Energy, **44** (2025) e14512. https://doi.org/10.1002/ep.14512.

UNCORRECTED PROOF

19. Harja M., Ciobanu G. – Studies on adsorption of oxytetracycline from aqueous solutions onto hydroxyapatite. Sci. Total Environ., **628–629** (2018) 36–43. https://doi.org/10.1016/j.scitotenv.2018.02.027.
20. Langmuir I. – The adsorption of gases on plane surfaces of glass, mica and platinum. J. Am. Chem. Soc., **40** (1918) 1361–1403. https://doi.org/10.1021/ja02242a004.
21. Freundlich H. – Über die adsorption in lösungen. Z. Phys. Chem. **57U** (1907) 385–470. https://doi.org/10.1515/zpch-1907-5723.
22. Redlich O., Peterson D. L. – A useful adsorption isotherm. J. Phys. Chem., **63** (1959) 1024–1024. https://doi.org/10.1021/j150576a611.
23. Luo J., Li X., Ge C., Müller K., Yu H., Huang P., Li J., Tsang D. C. W., Bolan N. S., Rinklebe J., et al. – Sorption of norfloxacin, sulfamerazine and oxytetracycline by KOH-modified biochar under single and ternary systems. Bioresour. Technol., **263** (2018) 385–392. https://doi.org/10.1016/j.biortech.2018.05.022.
24. Tian H., Peng S., Zhao L., Chen Y., Cui K. – Simultaneous adsorption of Cd(II) and degradation of OTC by activated biochar with ferrate: Efficiency and mechanism. J. Hazard. Mater., **447** (2023) 130711. https://doi.org/10.1016/j.jhazmat.2022.130711.
25. Jia M., Wang F., Jin X., Song Y., Bian Y., Boughner L. A., Yang X., Gu C., Jiang X., Zhao Q. – Metal ion–oxytetracycline interactions on maize straw biochar pyrolyzed at different temperatures. Chem. Eng. J., **304** (2016) 934–940. https://doi.org/10.1016/j.cej.2016.05.064.
26. Song J., Lu L., Wang J., Li X., Li J., Wang Q., Du H., Xin S., Xu L., Yan Q., et al. – Highly efficient nanocomposite of Y_2O_3@biochar for oxytetracycline removal from solution: Adsorption characteristics and mechanisms. Bioresour. Technol., **385** (2023) 129380. https://doi.org/10.1016/j.biortech.2023.129380.
27. Zhang H., Song X., Zhang J., Liu Y., Zhao H., Hu J., Zhao J. – Performance and mechanism of sycamore flock based biochar in removing oxytetracycline hydrochloride. Bioresour. Technol., **350** (2022) 126884. https://doi.org/10.1016/j.biortech.2022.126884.
28. Wu G., Ling H., Liu Y., Ma J., Zhang X., Li S., Wang Q., Li J., Wang X., Chen L. – Ambient dried metal organic frameworks aerogels with highly hydrophilic properties for fast adsorption removal of oxytetracycline. J. Hazard. Mater. Adv., **19** (2025) 100824. https://doi.org/10.1016/j.hazadv.2025.100824.
29. Zhang J., Xia X., Li K., Shen Y., Xue Y. – New insights into temperature-induced mechanisms of copper adsorption enhancement on hydroxyapatite-in situ self-doped fluffy bread-like biochar. Chem. Eng. J., **479** (2024) 147657. https://doi.org/10.1016/j.cej.2023.147657.
30. Sun Y., Wang X., Xia S., Zhao J. – New insights into oxytetracycline (OTC) adsorption behavior on polylactic acid microplastics undergoing microbial adhesion and degradation. Chem. Eng. J., **416** (2021) 129085. https://doi.org/10.1016/j.cej.2021.129085.
31. Khan A., Le Pivert M., Ranjbari A., Dragoe D., Bahena-Uribe D., Colbeau-Justin C., Herrero C., Rutkowska-Zbik D., Deschamps J., Remita H. – Cu-based MOF/TiO_2 composite nanomaterials for photocatalytic hydrogen generation and the role of copper. Adv. Funct. Mater., **36** (2025) 2501736. https://doi.org/10.1002/adfm.202501736.

UNCORRECTED PROOF